



Three-phase Evolution of a Coronal Hole. II. The Magnetic Field

Stephan G. Heinemann , Stefan J. Hofmeister , Astrid M. Veronig , and Manuela Temmer
University of Graz, Institute of Physics, Universitätsplatz 5, A-8010 Graz, Austria; stephan.heinemann@gmail.at

Received 2018 February 20; revised 2018 May 22; accepted 2018 June 29; published 2018 August 8

Abstract

We investigate the magnetic characteristics of a persistent coronal hole (CH) extracted from EUV imagery using Heliospheric and Magnetic Imager filtergrams over the period 2012 February–October. The magnetic field, its distribution, and the magnetic fine structure in the form of flux tubes (FTs) are analyzed in different evolutionary states of the CH. We find a strong linear correlation between the magnetic properties (e.g., signed/unsigned magnetic field strength) and the area of the CH. As such, the evolutionary pattern in the magnetic field clearly follows a three-phase evolution (growing, maximum, and decaying) as found from EUV data (Part I). This evolutionary process is most likely driven by strong FTs with a mean magnetic field strength exceeding 50 G. During the maximum phase they entail up to 72% of the total signed magnetic flux of the CH, but only cover up to 3.9% of the total CH area, whereas during the growing and decaying phases, strong FTs entail 54%–60% of the signed magnetic flux and cover around 1%–2% of the CH’s total area. We conclude that small-scale structures of strong unipolar magnetic field are the fundamental building blocks of a CH and govern its evolution.

Key words: Sun: corona – Sun: magnetic fields – Sun: photosphere

1. Introduction

Coronal holes (CHs) are large-scale structures in the solar corona consisting primarily of open magnetic field that is presumably rooted in the photosphere, and they are the major source of high-speed solar wind. The open magnetic field is usually dominated by one magnetic polarity, which is caused by a continuing imbalance in the local magnetic flux emergence (Levine 1982; Wang et al. 1996). Looking into the fine structure of the CH magnetic field, it is found that in local minima of flux emergence, i.e., between photospheric granulation cells, magnetic elements are accumulating into small-scale unipolar structures called flux tubes (FTs), network bright points, or solar filigree (Dunn & Zirker 1973; Berger & Title 2001; Cranmer 2009). They can be observed in line-of-sight (LoS) photospheric magnetograms as regions with areas of less than a few times 10^6 km^2 which entail the majority of the signed magnetic flux coming from a CH, and therefore may be considered as CH “footpoints” (e.g., Tu et al. 2005; Hofmeister et al. 2017).

In the higher atmospheric layers those small-scale magnetic structures coincide mostly with the edges and nodes of the chromospheric network cells and expand rapidly in the higher chromosphere to merge to a nearly homogeneous vertical magnetic field in the corona (Gabriel 1976; Dowdy et al. 1986). Funnels are open magnetic structures connecting the chromosphere with the solar corona (Hackenberg et al. 2000, and references therein). These so-called magnetic funnels have been suggested as the source regions of the high-speed streams (HSS) of solar wind within CHs (Hassler et al. 1999; Tu et al. 2005; Wiegmann et al. 2005).

However, not all of the magnetic flux in a CH is unipolar, and a significant number of closed field lines exist within its boundaries. Wiegmann & Solanki (2004) investigated the difference between CHs and the quiet Sun. It was found that, despite a relatively large amount of signed magnetic flux ($77\% \pm 14\%$), closed magnetic loops still exist. The average height of those loops is found to be lower in CHs than in the quiet Sun. This may be related to the funnel-like expansion of the FTs into the corona, which forms canopy-like regions between the funnels. The magnetic field as

well as magnetic funnels of CHs have been studied and modeled especially in relation to the acceleration mechanism of the solar wind at low solar heights (e.g., Levine 1982; Wang & Sheeley 1990; Gosling 1996; Wang 2009; Hofmeister et al. 2017), but details of the evolution of the magnetic field as well as the evolution of FTs in the context of CH evolution are still missing. As these intrinsic magnetic field properties of a CH shape not only the local field within the CH but also the global solar magnetic field (Bilenco 2002; Petrie & Haislmaier 2013; Wiegmann et al. 2014; Bilenco & Tavastsherna 2016), a detailed analysis of the evolution of a CH together with its underlying magnetic field is of great interest.

To investigate the photospheric magnetic field encompassed by the CH region, the boundaries of CHs need to be extracted. This is usually performed from hot coronal emission lines in the EUV and X-ray wavelength range. Owing to their low plasma density and temperature compared to the surrounding corona, CHs are observed at these wavelengths as dark structures and can be extracted with algorithms that are based on intensity thresholds (e.g., Schwenn 2006; Krista & Gallagher 2009; Rotter et al. 2012; Reiss et al. 2014; Hofmeister et al. 2017).

In the first part of this study (Heinemann et al. 2018, hereafter referred to as paper I) the evolution of a long-lived (10 solar rotations) and low-latitude CH was investigated using combined EUV image data and in situ measurements from three different viewpoints covering 360° of the heliosphere. With the usage of the two *STEREO* satellites (*Solar TErestrial RElations Observatories*; Kaiser et al. 2008) the CH could be seamlessly tracked over its entire lifespan, from which we derived a three-phase evolution (growing, maximum, decaying) of the CH. These phases were most prominently revealed in the evolution of the CH area but were also obtained from multiple other parameters (e.g., intensity, associated solar wind speed). In addition to the area, intensity, and parameters of the associated HSS, the rotational and latitudinal motion of the CH has also been analyzed in paper I.

The evolutionary pattern found in paper I is most likely related to the underlying magnetic field, and the present study will give a better understanding of the magnetic evolution. Limited to the view from Earth, we investigate the same long-lived low-latitude CH that

was studied in paper I, using data from the Heliospheric and Magnetic Imager (HMI, Schou et al. 2012; Couvidat et al. 2016) on board the *Solar Dynamics Observatory* (*SDO*, Pesnell et al. 2012). We analyze the change in the global CH magnetic field and its distribution as well as its fine structure in the form of FTs and relate it to the evolutionary structure of the CH as derived in paper I.

2. Data and Methods

2.1. Data

The HMI/*SDO* instrument acquires velocity, magnetic field, and spectral line measurements of the solar photosphere from narrowband filtergrams of six wavelengths centered on the spectral line of Fe I (6173 Å). Sequences are obtained every 45 s or 135 s with an image size of 4096×4096 pixel and an angular resolution of $0.^{\circ}5$ (Couvidat et al. 2016). For this study LoS magnetograms were used for the magnetic field measurements. The 720 s LoS data were used due to the lower photon noise of ~ 3 G measured near the center of the solar disk and because of the higher signal-to-noise ratio at lower field strengths in comparison to vector magnetograms.

To minimize projection effects, LoS magnetic field data were analyzed for each rotation of the CH around the time of the central meridian passage (CMP) of the CH's center of mass (CoM). This covers a spatial range of $\pm 10^{\circ}$ longitude from the central meridian and is related to a time window of roughly ± 18 hr around the time of the CMP of the CoM (assuming that the magnetic field does not change substantially over that period). For each rotation during that time window, data are taken at a 1 hr cadence and downloaded from the Joint Science Operations Center. This results in a data set of ~ 25 – 30 images per CMP. We calculate each parameter from each image and then average over each set to reduce noise and short-term variations. In total, this gives 10 data points for studying the magnetic field evolution of the CH.

2.2. Data Reduction and CH Extraction

Basic data reduction was applied using the SolarSoft Suite of the Interactive Data Language (SSW-IDL). The images were prepped to level 1.5 and bad images (e.g., saturation or high noise) were removed.

Using LoS magnetic field data, we assumed a radial magnetic field, which was corrected by applying a pixelwise correction:

$$B_{i,\text{corr}} = \frac{B_i}{\cos(\alpha_i)}, \quad (1)$$

with $B_{i,\text{corr}}$ being the corrected value of each pixel of the magnetic field map, B_i the uncorrected one, and α_i the respective angular distance from the center of the solar disk.

To analyze the magnetic field underlying the CH, we apply CH masks extracted from EUV images to the co-registered photospheric magnetic field maps. The CH boundaries were extracted from EUV 193 Å images from the Atmospheric Imaging Assembly (AIA, Lemen et al. 2012) by applying an intensity-based threshold method (35% of the median intensity of the solar disk; for more details see paper I).

The projection-corrected area was calculated from the binary CH maps under the assumption of a spherical Sun:

$$A_{i,\text{corr}} = \frac{A_i}{\cos(\alpha_i)}, \quad (2)$$

with A_i being the area per pixel and α_i the angle toward the center of the solar disk. From this we were able to calculate the size of

the CH by adding up the corrected areas for all CH pixels:

$$A = \sum_i^N A_{i,\text{corr}}. \quad (3)$$

The area is given in square kilometers.

In a similar way to that for the magnetic field, we average the calculated area in 1 hr cadence over a time window of ± 18 hr around the time of the CMP of the CoM (see Section 2.5 in paper I). The error bars shown in Figures 3, 6–8, and 10 are the 1σ standard deviations from the mean values.

2.3. Analysis of the Global Magnetic Field within the CH

The parameters of the global CH magnetic field, as extracted from the EUV mask, include the magnetic field strength, the magnetic flux, and the magnetic field distribution with its moments (mean, variance, skewness, and kurtosis).

The mean (signed) magnetic field strength \bar{B} , in gauss [G] was calculated as

$$\bar{B} = \frac{1}{N} \sum_i^N B_{i,\text{corr}}, \quad (4)$$

where i represents the i th pixel of the CH and N is the total number of pixels within the CH. Correspondingly, the unsigned magnetic field strength is calculated as

$$\bar{B}_{\text{us}} = \frac{1}{N} \sum_i^N |B_{i,\text{corr}}|. \quad (5)$$

From the magnetic field strength and the area of the structure we can derive the magnetic flux, Φ . The magnetic flux is given in maxwell [Mx] and can be divided into signed (or *open*) and unsigned (or *total*) flux. The signed magnetic flux Φ_s is calculated as the net flux through the respective area:

$$\Phi_s = \sum_i^N (B_{i,\text{corr}} A_{i,\text{corr}}), \quad (6)$$

with B_i and A_i the magnetic field strength and area for each pixel respectively. The unsigned magnetic flux Φ_{us} is calculated as the total flux through the respective area:

$$\Phi_{\text{us}} = \sum_i^N (|B_{i,\text{corr}}| A_{i,\text{corr}}). \quad (7)$$

From the signed and unsigned magnetic flux we can define the magnetic flux balance R_Φ of a CH as

$$R_\Phi = \frac{|\Phi_s|}{\Phi_{\text{us}}}. \quad (8)$$

The signed flux divided by the unsigned flux of a CH can be seen as a measure of the flux that is not balanced within the CH, and this provides a measure of the percentage of open flux.

2.4. FT Extraction and Analysis

To analyze the fine structure within the CH that is composed of FTs, i.e., small-scale unipolar structures, we use a simple threshold-based method that is applied to the magnetograms with a threshold value of ± 20 G. All structures with pixels above this threshold and containing at least three pixels were extracted as FTs. The value of ± 20 G was chosen because structures extracted with this and with higher thresholds show unipolar properties,

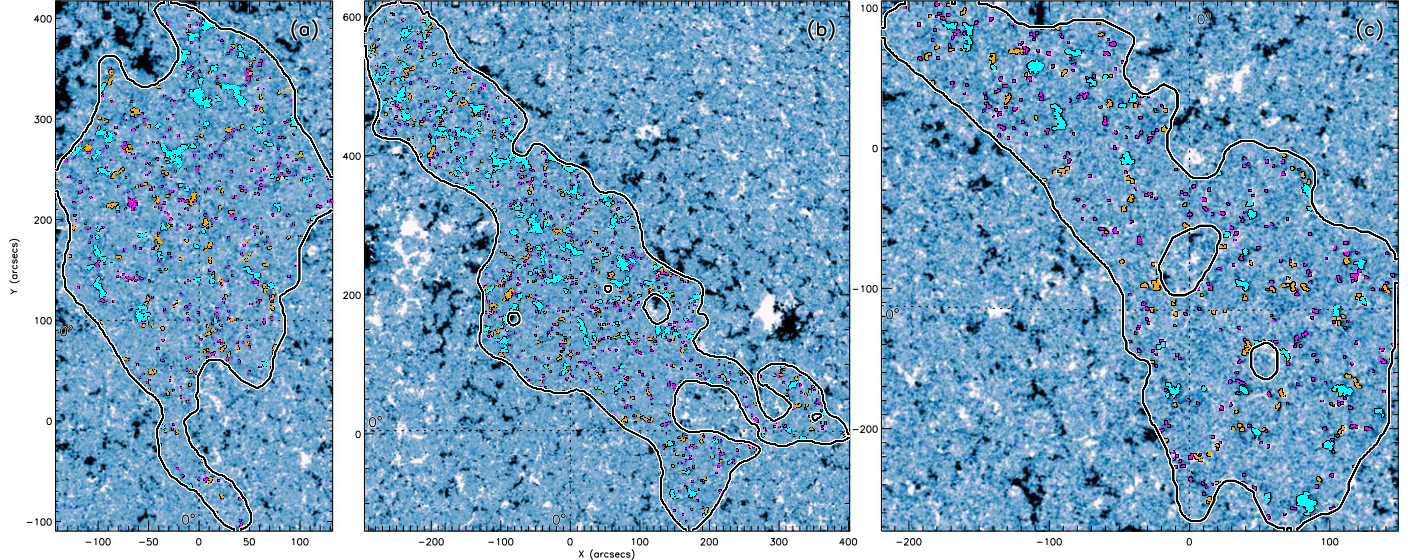


Figure 1. Photospheric magnetograms, scaled to ± 20 G with the CH boundary overlaid (black) and with contours of FTs of different categories. The cyan contours show the strong FTs, the orange the medium FTs, and the magenta the weak FTs. The panels represent different stages of the CH evolution (left: growing phase, 2012 April 9; middle: maximum phase, 2012 June 3; right: decaying phase, 2012 August 22). Note that each image has a different axis-scaling, representing different zoom levels of the magnetogram.

whereas structures that have been extracted with a lower threshold may also contain pixels with opposite polarity (see also Hofmeister et al. 2017). The value for the average unipolarity for all FTs extracted is $0.99^{+0.01}_{-0.02}$, which gives support for the choice of the threshold of 20 G. The unipolarity (or magnetic flux balance) is calculated using Equation (8) as described in Section 2.3; for values around 1, it indicates that all pixels of the structure (i.e., the FT) are of the same polarity.

The total number of extracted FTs is called the FT ensemble. This ensemble is then sorted into three categories based on the absolute value of the mean magnetic field strength of each FT structure $|\bar{B}_{\text{FT}}|$, which is calculated as

$$|\bar{B}_{\text{FT}}| = \frac{1}{N} \sum_i^N |\bar{B}_{i,\text{corr}}|, \quad (9)$$

where i represents the i th pixel of the FT and N is the total number of pixels that make up the FT.

FTs in the first category have the lowest magnetic field strengths and are called *weak* FTs. If the absolute value $|\bar{B}_{\text{FT}}|$ of an FT is between 20 and 35 G it is placed into the pool of weak FTs. The next category are the *medium* FTs, which have an absolute value of the mean magnetic field strength between 35 and 50 G. All FTs that have a mean magnetic field strength exceeding ± 50 G are called *strong* FTs. Figure 1 shows three snapshots of the CH magnetic field (one of each phase) with the FTs highlighted. The *strong* FTs are shown in cyan, the *medium* FTs in orange, and the *weak* FTs in magenta. The FTs seem to be aligned along the magnetic network (Gabriel 1976; Dowdy et al. 1986), and a change in the relative abundance of the FTs during the CH evolution can be seen.

The area of each FT is calculated using

$$A_{\text{FT}} = \sum_i^N A_{i,\text{corr}}, \quad (10)$$

with $A_{i,\text{corr}}$ being the area of each FT pixel corrected for a spherical Sun (Equation (2)) and N the number of pixels of the FT. The flux for each FT was calculated using Equations (6) and (7). By summing over all FTs of one category in one image, we can calculate the FT property of the total CH, e.g.,

Table 1
Overview of Parameters Defined in Section 2

Parameter	Definition ^{a,b}	Description
A	$= \sum_i A_i$	Area
\bar{B}	$= \frac{1}{N} \sum_i B_i$	Signed mean magnetic field strength
\bar{B}_{us}	$= \frac{1}{N} \sum_i B_i $	Unsigned mean magnetic field strength
Φ_s	$= \sum_i (B_i A_i)$	Signed magnetic flux
Φ_{us}	$= \sum_i (B_i A_i)$	Unsigned magnetic flux.
R_{Φ}	$= \frac{\Phi_s}{\Phi_{\text{us}}}$	Flux balance, ratio of signed to unsigned magnetic flux
r_{Φ}	$= \frac{ \Phi_{\text{FT}} }{\Phi_{\text{CH}}}$	Flux ratio, ratio of flux from FTs to the CH flux
r_A	$= \frac{ A_{\text{FT}} }{A_{\text{CH}}}$	Area ratio, ratio of area of FTs to the CH area

Notes.

^a Note that A_i and B_i represent the corresponding corrected versions $A_{i,\text{corr}}$ and $B_{i,\text{corr}}$.

^b Properties of coronal hole and flux tube are denoted with the subscripts CH and FT respectively.

$\Phi_{\text{FT},s}$ is the signed flux coming from all (weak, medium, or strong) FTs within the CH.

Lastly we can define the FT proportions—the area proportion and the flux proportion. These ratios show how much a certain category of FTs contributes to the respective parameter of the total CH in terms of flux or area:

$$r_{\Phi} = \left| \frac{\Phi_{\text{FT}}}{\Phi_{\text{CH}}} \right| \quad (11)$$

$$r_A = \frac{|A_{\text{FT}}|}{A_{\text{CH}}}$$

The correlation between the various extracted parameters is calculated using the Pearson correlation coefficient and the Spearman correlation coefficient. To consider the significance of the relation for a low number of data points, we apply a bootstrapping algorithm (Efron & Tibshirani 1993; Efron 1979) to the data set with over 10^6 repetitions (replacement for each repetition is taken from the initial set, with each data point in

this subset coming from a Gaussian distribution of itself plus its standard deviation). The correlation coefficients are calculated from the derived subsets and given as mean values of all repetitions. The confidence intervals (CIs) for the correlation coefficients (90%, 95%, 99%) were calculated using the respective quantiles. An overview of the parameters defined in this section is given in Table 1. A summary of all results and statistical parameters is given in Table 2 in the Appendix.

3. Results on Magnetic Properties of a CH

In this section, we present the results of the evolution of the magnetic field properties of the CH under study. Snapshots of the evolution over the entire lifespan of the CH are shown in Figure 2 with the full-disk magnetograms and CH contours overlaid in black.

3.1. Area and Magnetic Field Strength

In the following, we take up the result of paper I where we show the three-phase evolution of the CH as derived from the evolution of its area (and other parameters such as the intensity and the in situ peak velocity of the associated HSS of the solar wind). Figure 3(a) shows the evolution of the CH area as observed from Earth together with the evolution of the mean magnetic field strength of the CH over its lifetime. From the CH area (dashed black line) we clearly obtain the three-phase evolutionary pattern. In the growing phase, lasting from 2012 February 4 until 2012 May 13, we see a first peak in the deprojected area at $\sim 6 \cdot 10^{10} \text{ km}^2$ followed by a fast decline to $\sim 2 \cdot 10^{10} \text{ km}^2$ and a growth until a maximum is reached. The maximum phase settles at an area of $\sim 9 \cdot 10^{10} \text{ km}^2$ around 2012 June 3 and lasts about one month. In the decaying phase the area drops first sharply then moderately to $\sim 1 \cdot 10^{10} \text{ km}^2$ until the CH can no longer be observed in 2012 October. The error bars represent the 1σ deviation from the averaging as described in Section 2. The three phases are marked by the color bar at the bottom of Figure 3(a).

For comparison, we also plot in Figure 3(a) the evolution of the signed magnetic field strength (blue line), representing a measure of the open field within the CH, and the unsigned field strength (red line), measuring the absolute field strength. From this we see a synchronized evolutionary behavior that seems to be linked to the evolution of the CH area; nevertheless some differences are obtained. The mean field strength varies between -1 and -5 G, hence the predominant negative polarity does not change over the CH lifetime. The profile shows one early peak (-2.7 G) around 2012 April 9, which does not match the CH evolution, and a main peak (-4.4 G) around 2012 June 3 that coincides with the peak in the area. During the maximum phase the signed mean magnetic field strength declines to -3.8 G before dropping significantly at the start of the decaying phase. In the decaying phase the value drops below -1 G. The unsigned mean magnetic field strength shows a similar behavior to the signed field strength. It reveals an early peak (6.7 G) during the growing phase of the CH area, as well a clear maximum (8.6 G) and a decrease to 5.6 G that both match the CH evolution.

Figure 3(b) explores the relation of the signed field strength to the area. We find a linear correlation with a Pearson correlation coefficient of $c = -0.82$ with a 95% CI of $[-0.36, -0.97]$. The linear regression fit for this CH can be expressed as

$$A = (-1.21 \pm 0.33) + (-2.46 \pm 0.16)\bar{B}. \quad (12)$$

The area A is given in 10^{10} km^2 and the mean magnetic field strength \bar{B} is given in gauss. A similar significant relation can be

found when comparing the unsigned mean magnetic field strength to the CH area (Figure 3(c)), where we find a linear correlation with a Pearson correlation coefficient of $c = 0.83$ in a 95% CI of $[0.38, 0.97]$. The linear regression fit can be described as

$$A = (-14.22 \pm 1.25) + (2.88 \pm 0.19)\bar{B}_{\text{us}}. \quad (13)$$

3.2. Magnetic Field Distribution

Figure 4 shows the normalized magnetic field pixel distribution for five time steps, each corresponding to one data point in Figure 3, representing different stages in the evolution of the CH. The first two lines (green, dark green) mark the growing phase around 2012 March 13 and May 6. The red line is the magnetic field distribution during the maximum around 2012 June 3. The blue lines (dark blue, blue) represent the decaying phase around 2012 July 26 and September 18. The distribution follows a Lorentzian-like profile that is shifted to the dominant polarity of the CH (between -0.25 and -0.5 G). By comparing the distributions of the different evolutionary stages we find a broadening from the growing to the maximum phase. We find an increase in the density of pixels with higher field strengths (flanks of the distribution) in the maximum phase compared to the growing and decaying phases.

Figure 5 shows the second, third, and fourth moments of the magnetic field distribution, corresponding to the standard deviation (square root of the variance), the skewness (a measure of the lopsidedness of a distribution), and the kurtosis (a measure of the heaviness of the tail of the distribution). Interestingly, we find a similar behavior in all the profiles: a clear peak in the maximum phase followed by a steep drop to low values in the decaying phase. This suggests a significant change in the magnetic field distribution in the maximum phase, which coincides with the maximum in the area. The asterisks represent the last data point (around 2012 October 14), which we excluded as an outlier in calculating the moments of the distribution, because of large uncertainties in the extraction and deprojection of the magnetic field with a small area. The outlier value arises from a few erroneously detected CH pixels, which cover strong fields. Due to the small CH area at this time, these erroneous pixels greatly alter the calculated moments of the distribution.

3.3. Magnetic Flux

Figure 6 shows the CH's signed flux Φ_s , unsigned flux Φ_{us} , and the flux balance (Φ_s/Φ_{us}). The unsigned flux has a negative polarity, but for visualization purposes in Figure 6 the absolute value is plotted. The fluxes show the same trend as the area and the mean magnetic field strength, with growing, maximum, and decaying phases. The signed flux (red) peaks at a maximum of $4 \cdot 10^{21} \text{ Mx}$ and reaches down to $1 \cdot 10^{21} \text{ Mx}$ during the CH "formation" and decay phase. The unsigned flux (blue) peaks at the same time as the signed flux with $8 \cdot 10^{21} \text{ Mx}$ and ranges down to $1.5 \cdot 10^{21} \text{ Mx}$. The flux balance also peaks during the maximum phase with a flux balance of 0.5, and it ranges down to 0.2 during the early and late phases. The variation within the CH area correlates with the variation of magnetic flux and clearly shows the three-phase evolution.

4. FT Properties

In contrast to the global magnetic characteristics of the photospheric field covered by the CH that are presented in Section 3, here we analyze the magnetic fine structure within the

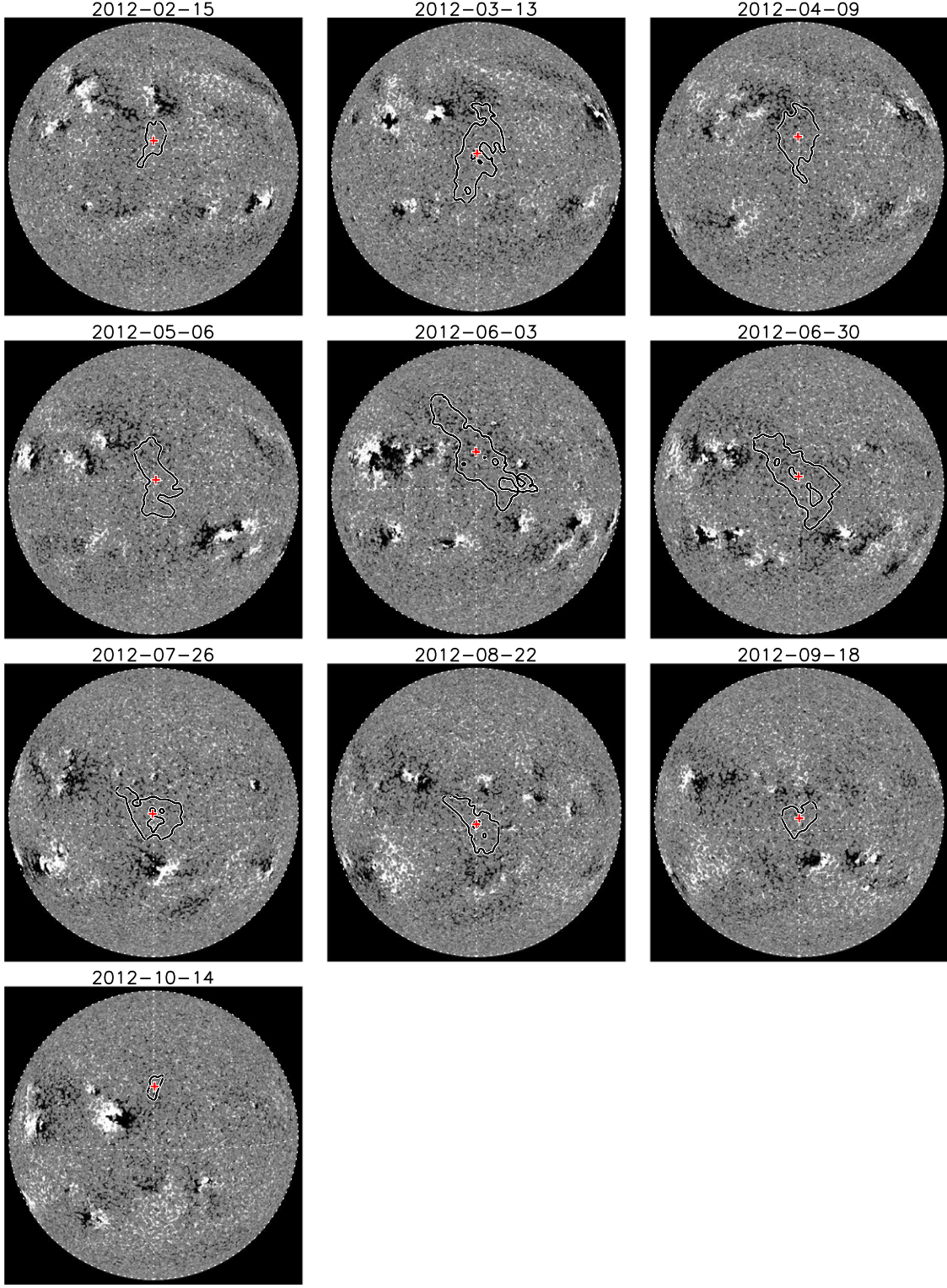


Figure 2. Evolution of the LoS magnetic field below the CH during its lifetime over 10 solar rotations. HMI full-disk LoS magnetograms are shown with black contours representing the CH boundaries extracted from the AIA images and the red cross showing the CoM of the CH.

CH, which is known to be clustered in FTs, small-scale magnetic structures of unipolar flux (Tu et al. 2005; Hofmeister et al. 2017).

4.1. Proportions of FT Number and Area

Figure 7(a) shows the evolution of the average number of FTs in the CH separately for the three different FT categories, namely weak (magenta), medium (orange), and strong FTs (cyan). The

number of strong FTs ranges from 7 to over 160, the number of medium FTs from 12 to 230, and the number of weak FTs from 40 to 870. Although weak FTs appear most frequently during the whole evolution, the strong FTs have the highest area proportion, i.e., the area of all FTs of one category in comparison to the total area of the CH (Figure 7(b)). During the maximum phase, strong FTs cover up to 3.9% of the total CH area. During growing and decaying phases this number is up to a factor of 3 lower.

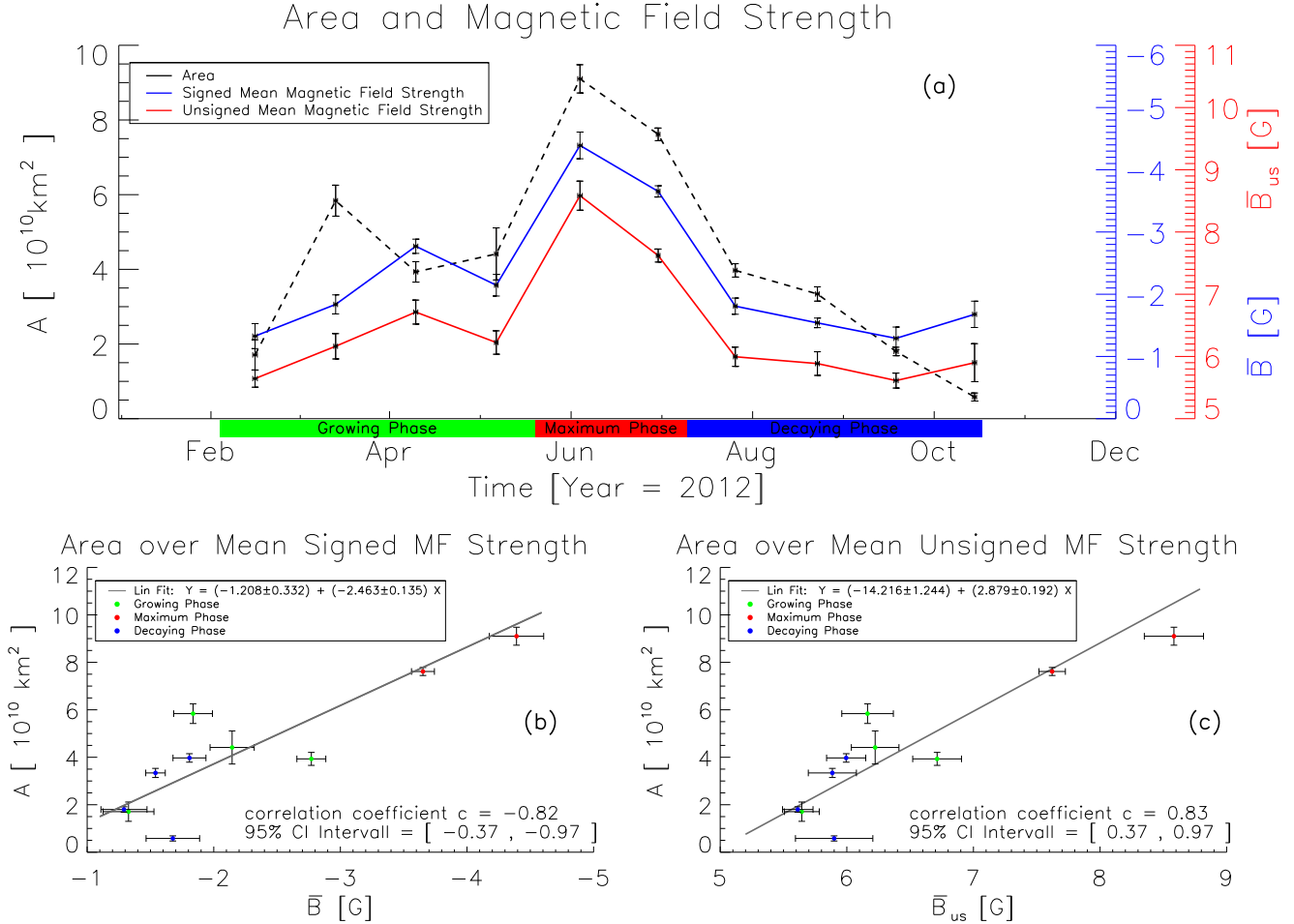


Figure 3. (a) Evolution of the area (dashed, black), the signed mean magnetic field strength (blue) and the unsigned mean magnetic field strength (red) of the CH. (b) Correlation between signed mean magnetic field strength and area. (c) Correlation between unsigned mean magnetic field strength and area. The colored data points (green, red, and blue) show their affiliation with an evolutionary phase (growing, maximum, and decaying).

Variations in the area proportion of the other FT categories (weak, medium) are barely given, although their number does vary slightly following the three-phase evolution. Their area proportion averages around $(1.0 \pm 0.3)\%$. Figure 1 illustrates the evolution of the FT number and area proportion in three snapshots (one of each phase). Note that these findings also imply that strong FTs make the highest contribution to the total CH flux, because their field strength and their area proportion are the largest. This indicates that strong FTs play a major role in the evolution of a CH.

The number of FTs and the total area they cover show the three-phase evolution, therefore a relation would seem reasonable. Figure 8 shows the correlation between FT number and CH area using different colors for the different FT categories (weak FTs: magenta; medium FTs: orange; strong FTs: cyan). For weak FTs, we find a Pearson correlation coefficient of $c = 0.89$ with a 95% CI of $[0.62, 0.99]$. Although this reveals a high correlation, we note that the linear fit does not cover three data points (including error bars), making the correlation less significant. The medium FTs, however, have a more significant correlation. The Pearson correlation coefficient is $c = 0.96$ with a 95% CI of $[0.85, 0.99]$, and the linear fit can be described by

$$N = (-2.5 \pm 8.1) + (26.8 \pm 1.6)A \quad [10^{10} \text{ km}^2]. \quad (14)$$

For the strong FTs we see the strongest correlation with a Pearson correlation coefficient of $c = 0.96$ and a 95% CI of

$[0.89, 0.99]$, and the linear fit can be expressed as

$$N = (-7.1 \pm 4.7) + (17.4 \pm 0.9)A \quad [10^{10} \text{ km}^2]. \quad (15)$$

4.2. FT Distribution

Figure 9 shows the magnetic field distribution of FTs per area of different stages in the CH evolution. The color indices match Figure 4: the first two lines (green, dark green) represent the growing phase around 2012 March 13 and May 6. The red line is the magnetic field distribution during the maximum around 2012 June 3. The blue lines (dark blue, blue) represent the decaying phase around 2012 July 26 and September 18. From this we find clear differences between the distributions of the three phases. Besides the obvious and expected asymmetry of the distributions, due to one dominant polarity, the peak of the distribution in the growing phase is slightly lower than in the following phases. Toward the maximum phase the dominant (negative) polarity of the distribution rises, especially the flanks (i.e., at high field strengths), whereas the flank for FTs of the non-dominant polarity declines. We find a significant rise in the FTs below -70 G, which shows that strong FTs cause the main difference between the distributions. The decaying phase is marked by a decline of the dominant polarity flank and an increase of the non-dominant polarity flank. The number of weaker FTs does not change significantly (see also Figure 7).

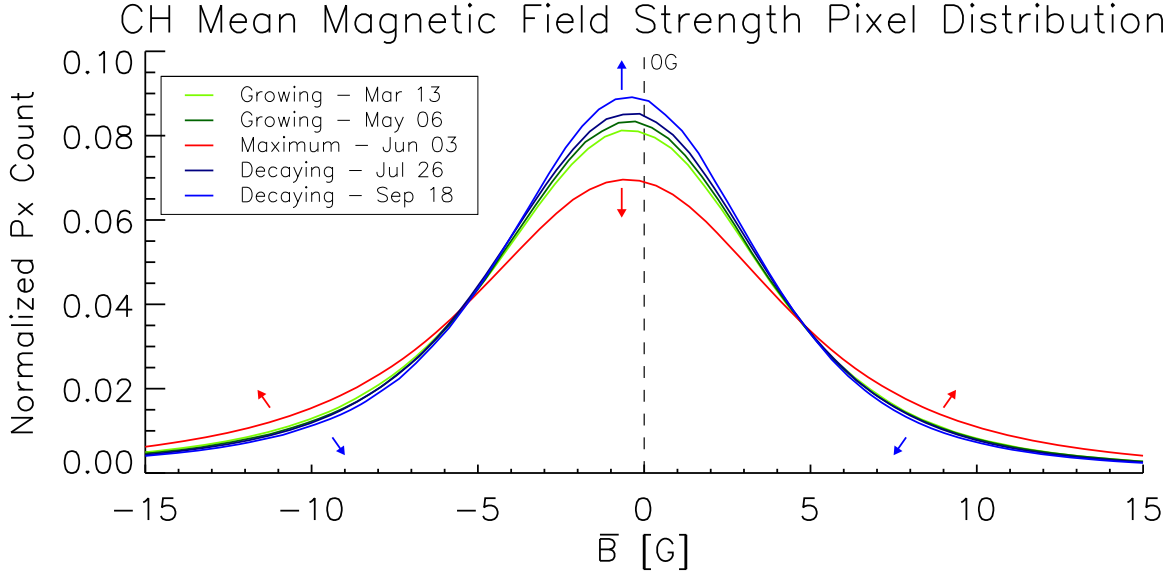


Figure 4. Probability distribution of magnetic field strength of all pixels within the CH. The different lines represent different stages in the evolution of the CH. The green lines (green, dark green) represent the growing phase around 2012 March 13 and May 6. The red line is the magnetic field distribution during the maximum around 2012 June 3. The blue lines (dark blue, blue) represent the decaying phase around 2012 July 26 and September 18.

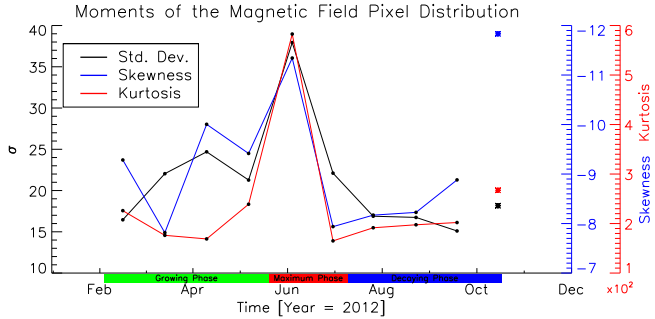


Figure 5. Moments of the magnetic field distribution of the CH. The standard deviation (square root of the second moment) is represented by the black line. The blue and red lines show the skewness (third moment) and kurtosis (fourth moment) respectively. The asterisks represent the last point, which was excluded due to large uncertainties (see text).

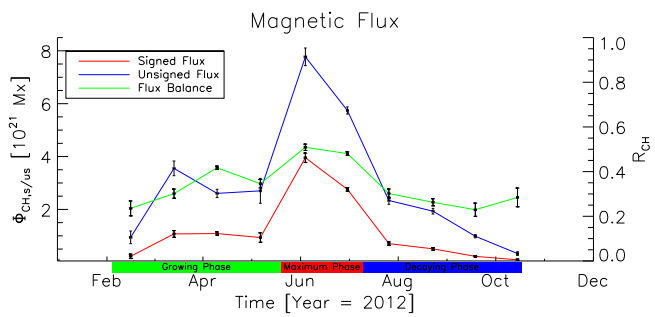


Figure 6. The signed (red) and unsigned (blue) magnetic flux and their ratio, the magnetic flux balance (green). Note that the absolute value of unsigned flux is plotted.

4.3. FT Flux Proportion

Figure 10 shows how much flux the FTs supply to the total signed flux of the CH, which may act as a measure of the *open* flux of the CH. We assume that flux from FTs of opposite polarity cancels within the CH. We find that a large fraction of the signed flux of the CH comes from FTs (70%–80%), which occupy less than 7% of the CH’s area. The major part of the flux comes from strong FTs (48%–71%). In the evolution of FT flux proportion,

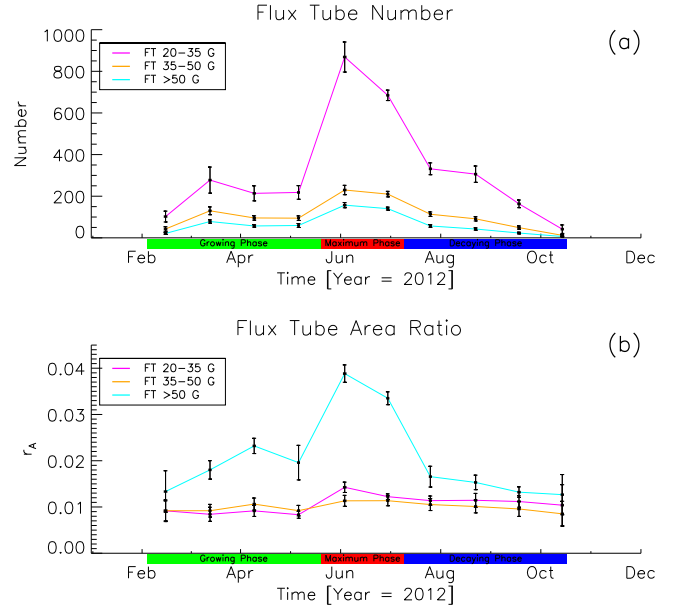


Figure 7. Evolution of the number of FTs (a) and of the ratio of the summed FT area and total CH area (b) in different FT categories, represented by different colors: magenta: weak FTs; orange: medium FTs; cyan: strong FTs.

the three-phase evolution is emphasized. We see the three distinctive phases as clearly as in the area, especially in the strong FTs. For strong FTs we have a constant flux proportion of 60% in the growing phase, which rises to ∼70% in the maximum phase and drops to around 54% in the decaying phase. It is also interesting to note that during the maximum phase the rise in contribution of the strong FTs is accompanied by a drop in the contribution of the medium FTs. Other than that, the contribution of the medium FTs (6%–14%) and the weak FTs (2.5%–4.5%) plays only a minor role in comparison to the strong FTs.

5. Discussion

Using photospheric LoS magnetograms, we have investigated the magnetic field evolution within a long-lived low-latitude CH

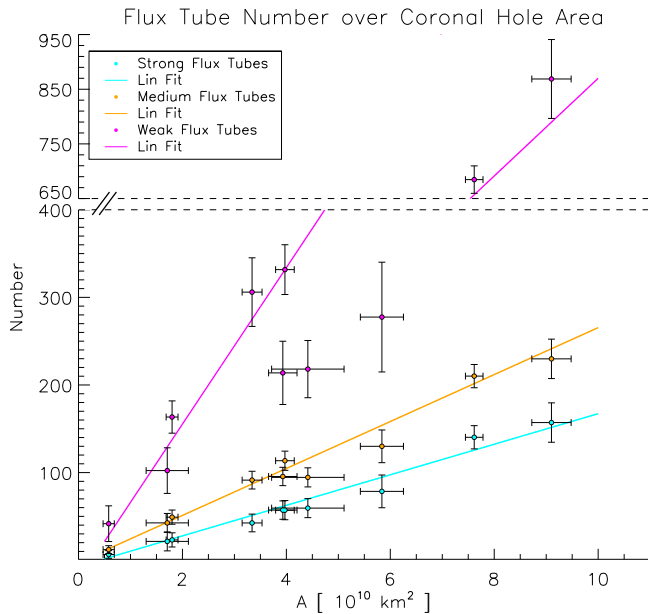


Figure 8. Correlation between the number of flux tubes and the CH area. The colors represent the different flux tube categories: magenta: weak FTs; orange: medium FTs; cyan: strong FTs.

over its entire lifetime of more than 10 solar rotations. The three-phase evolution as found in the CH area, intensity, and solar wind parameters of the associated HSS (see paper I) can also clearly be seen from the magnetic evolution of the underlying photospheric field of the CH. Small structures of unipolar field (strong FTs) are found to be the major contributor of signed flux (open magnetic field) within the CH and therefore play a key role in the magnetic evolution of the CH.

Our analysis of the CH magnetic field yields that the mean magnetic field strengths of both the signed and the unsigned fields peak at the same time as the CH area, with maxima of -4.4 G and 8.6 G respectively (Figure 3). The evolution of the CH area and that of the field strength are highly correlated, $c > 0.80$. For the magnetic flux (Figure 6) we can also see the rise to a maximum of $4 \cdot 10^{21} \text{ Mx}$ (signed flux) and $8 \cdot 10^{21} \text{ Mx}$ (unsigned flux). The fraction of the unbalanced (open) flux reaches a maximum of 50%. We find our results to be in good agreement with the statistical analysis of 288 low-latitude CHs by Hofmeister et al. (2017). This shows that the case study presented here is well reflected in statistical results (we note that the CH under study is a subset of the CHs used in the statistical study).

We find an evolutionary pattern in the magnetic field distribution of the CH, with the greatest changes in the flanks of the distribution. While the mean magnetic field strength, magnetic flux, and area have increased values over the entire maximum phase, the distribution reveals a major change around 2012 June 3 (Figures 4 and 5). We find a decrease in pixels of strong magnetic field ($>35 \text{ G}$) in the non-dominant polarity and an increase in pixels of strong magnetic field in the dominant polarity. The normalized core of the magnetic field distribution, however, stays very constant (Lorentz-like). This time period in the evolution of the CH seems to mark the turning point in the magnetic evolution, the evolutionary peak.

The importance of the magnetic fine structure of a CH with regard to its evolution becomes apparent when considering that FTs are the major contributor to the signed magnetic flux of the CH. Up to 80% of the CH's signed flux comes from less than 7% of its area. The FTs, which most likely form through flux accumulation at

the edges of the magnetic network (Gabriel 1976; Dowdy et al. 1986), expand into the corona, shaping and forming the coronal structure that is observed. The FT expansion is related to the magnetic field strength (e.g., Wang & Sheeley 1990; Tu et al. 2005; Cranmer 2009), hence changes are supposed to have a visible effect in the corona. Major changes in the distribution of the mean magnetic field strength are found for strong FTs (see Figure 9). Strong FTs are the most important because they contribute up to 70% to the total signed flux of the CH, but only cover $<5\%$ of the CH area, and their evolution is closely related to the evolution of the CH area. A similar conclusion was drawn from a statistical study by Hofmeister et al. (2017), who found that strong FTs are the major contributor to the signed magnetic flux of a CH.

In paper I of this case study, we have shown that the CH properties are different in the growing and decaying phases of the CH. This was derived especially for the CH area and the peak bulk velocity (v_p) of the corresponding HSS measured in situ at about 1 au. In this paper we find such a behavior also for the magnetic field distribution of the CH (Figure 9). The reason might be differences in the dynamic changes of flux emergence and outflow of solar wind plasma (growing phase) as well flux cancellation (decaying phase). We suspect that the process of growing might be linked to the contribution of the internetwork to the magnetic network (Gošić et al. 2014), which in CHs is usually dominated by one polarity (Levine 1982; Wang et al. 1996). The flux is then fed into the nodes of the magnetic network, which is built up by FTs, preferably through the merging of magnetic elements (Iida et al. 2012). Also a second process, the possible induction of magnetic field caused by vortices of outflowing plasma, is worth mentioning. From observations and simulations it has been shown that small-scale dynamos can form and induce magnetic field (e.g., see Petrovay & Szakaly 1993; Schüssler & Vögler 2008; Pietarila Graham et al. 2010; reviews by Solanki 1993; Schüssler 2013). In both cases, an increasing field strength in the FTs results in a larger FT diameter. As FTs strive to be in a pressure equilibrium with the surrounding plasma, an increase in magnetic field strength increases the magnetic pressure, which causes an expansion of the magnetic structure until the magnetic pressure and the outside gas pressure are equalized. When increasing the FT size, the catchment area for magnetic elements may also increase, which would lead to a faster accumulation of flux. Consequently, an increased FT diameter may increase the possible plasma outflow. In return, this may increase the magnetic field strength. Thus, the growth of FTs (in both area and magnetic field strength) might be due to a positive feedback loop between the magnetic field and the outflowing plasma.

For the decaying phase, we speculate that the closing processes might either be caused by supersurface phenomena such as the reconnection of open fields or/and a disruption of the positive feedback loop that grows and sustains the FTs. The efficiency of those closing processes may also be related to the configuration state of the magnetic field structure within the CH, meaning that different configurations facilitate growing and decaying processes differently. For example, if the continuous outflow in some funnels is disrupted and starts to weaken in a non-uniform or unsynchronized manner and at a higher rate than the increase in other funnels, we would expect a nonlinear relation between CH area and the outflow speed of the solar wind (which has been shown statistically, e.g., by Temmer et al. 2018).

The growth and decay of the overall CH might be related to the actual magnetic and gas pressure in the CH, which is strongly determined by the properties of the FTs as compared to the ambient corona. The total pressure gradient in the CH, and in

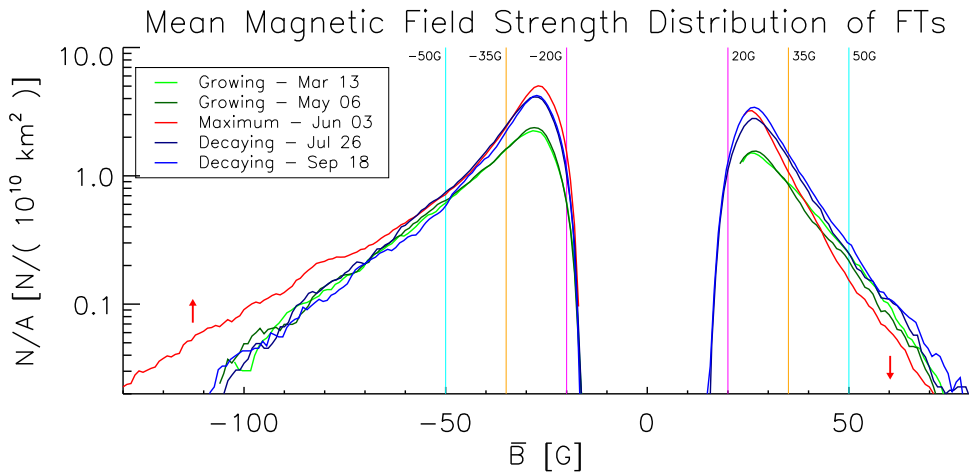


Figure 9. Distribution of FTs as a function of their mean magnetic field strengths during the CH evolution.

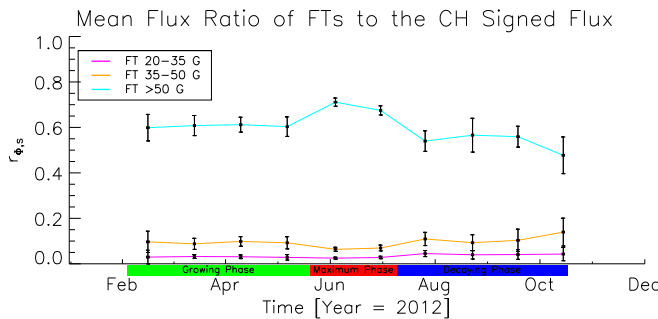


Figure 10. Flux contribution of the FTs to the signed flux in the CH. The different colors represent different FT categories: magenta: weak FTs; orange: medium FTs; cyan: strong FTs.

particular at the boundary of the CH, could lead to an effective expansion, respectively decay, of the CH. The evolution of the mean magnetic field strength is shown in Figure 3 and the mean intensity, which can be taken as a proxy for the gas pressure (because the intensity is determined by the density and temperature of the emitting plasma), is shown in paper I, Figure 8.

Our results not only increase our understanding of the evolution of a CH, but give valuable insights into their structure and may help to improve CH models, especially in combination with the modeling of the fast solar wind. The FTs (or their photospheric footpoints) may serve as boundary conditions to FT-based coronal and solar wind models (e.g., see Tu et al. 2005; Woolsey & Cranmer 2014; Pinto et al. 2016; Pinto & Rouillard 2017).

6. Conclusions

We have investigated the magnetic evolution of a chosen long-lived low-latitude coronal hole. The major findings can be summarized as follows.

1. We find a strong correlation between the CH area and the magnetic field strength that persists over the evolution of the CH, which shows the three-phase evolution proposed in Heinemann et al. (2018). The signed magnetic field strength increases during the growing phase of the CH from -2 G up to a peak of -4.4 G in the maximum phase. The peak corresponds to the peak in the CH area. The decaying phase is determined by a steep drop to below -2 G. The unsigned mean magnetic field strength shows a

nearly identical behavior with a maximum of 8.6 G and is below 6 G in the growing and decaying phases.

2. At the maximum of the CH area as well as at the maximum of magnetic field strength and flux we can derive a turning point of the evolution from the magnetic field distribution of the CH. The moments of the distributions also show a maximum there. We find an asymmetrical, Lorentzian-like profile that changes significantly in its flanks, with the core staying nearly unaffected.
3. We find that the magnetic field of a CH is composed of FTs that are linked to the magnetic network. The strong FTs ($>|50$ G) dominate the total magnetic flux of the CH. These FTs contribute $48\%-71\%$ to the total signed flux of the CH, despite covering less than 5% of the CH area. The percentage contribution of signed magnetic flux ($\approx 80\%$) and area ($\approx 7\%$) from FTs to the total CH signed (open) magnetic flux and area is maximal during the maximum phase of the CH evolution.

Our case study of a long-lived CH clearly shows that magnetic FTs are the elementary building blocks governing the CH evolution. Notably, during its maximum phase, the distribution of strong FTs of the dominant polarity reveals a strong intensification and governs the overall magnetic CH characteristics. Comparing these findings to the results in paper I, we also note that strong changes in the magnetic fine structure of the CH are reflected in a change of the characteristics of the associated high-speed solar wind streams.

The *SDO/AIA* and *SDO/HMI* image data are available courtesy of NASA/*SDO* and the respective science teams. We acknowledge the support by the FFG/ASAP Program under grant No. 859729 (SWAMI). A.M.V. and M.T. acknowledge the Fonds zur Förderung wissenschaftlicher Forschung (FWF): P24092-N16 and V195-N16. S.J.H. acknowledges support from the JungforscherInnenfonds der Steiermärkischen Sparkassen.

Appendix

Table 2 gives detailed results of the Pearson and Spearman correlation coefficients calculated for the magnetic field strength—area relations (both signed and unsigned) as well as the area—FT number relations. The method and calculation of the coefficients is found in Section 2.4.

Table 2
Overview of Correlation Coefficients

Relation	Figure	Pearson Correlation Coefficient				
		μ_p	σ_p	CI 90%	CI 95%	
\bar{B}_s versus A_{CH}	3(b)	-0.82	0.15	[-0.48, -0.96]	[-0.37, -0.97]	[-0.15, -0.99]
\bar{B}_{us} versus A_{CH}	3(c)	0.84	0.14	[0.54, 0.97]	[0.42, 0.97]	[0.20, 0.99]
A_{CH} versus $N_{FT, \text{strong}}$	8	0.96	0.03	[0.91, 0.99]	[0.89, 0.99]	[0.83, 1.00]
A_{CH} versus $N_{FT, \text{medium}}$	8	0.96	0.04	[0.88, 0.99]	[0.85, 0.99]	[0.75, 1.00]
A_{CH} versus $N_{FT, \text{weak}}$	8	0.89	0.10	[0.71, 0.98]	[0.62, 0.99]	[0.35, 1.00]

Relation	Figure	Spearman Correlation Coefficient				
		μ_s	σ_s	CI 90%	CI 95%	
\bar{B}_s versus A_{CH}	3(b)	-0.73	0.18	[-0.38, -0.94]	[-0.27, -0.95]	[-0.06, -0.98]
\bar{B}_{us} versus A_{CH}	3(c)	0.74	0.17	[0.41, 0.95]	[0.31, 0.96]	[0.09, 0.99]
A_{CH} versus $N_{FT, \text{strong}}$	8	0.91	0.08	[0.76, 0.99]	[0.70, 0.99]	[0.54, 1.00]
A_{CH} versus $N_{FT, \text{medium}}$	8	0.88	0.11	[0.67, 0.98]	[0.60, 0.99]	[0.39, 1.00]
A_{CH} versus $N_{FT, \text{weak}}$	8	0.78	0.18	[0.43, 0.96]	[0.32, 0.98]	[0.06, 0.99]

ORCID iDs

Stephan G. Heinemann [ID](https://orcid.org/0000-0002-2655-2108) <https://orcid.org/0000-0002-2655-2108>
Stefan J. Hofmeister [ID](https://orcid.org/0000-0001-7662-1960) <https://orcid.org/0000-0001-7662-1960>
Astrid M. Veronig [ID](https://orcid.org/0000-0003-2073-002X) <https://orcid.org/0000-0003-2073-002X>
Manuela Temmer [ID](https://orcid.org/0000-0003-4867-7558) <https://orcid.org/0000-0003-4867-7558>

References

- Berger, T. E., & Title, A. M. 2001, *ApJ*, **553**, 449
Bilenko, I. A. 2002, *A&A*, **396**, 657
Bilenko, I. A., & Tavastsherna, K. S. 2016, *SoPh*, **291**, 2329
Couvidat, S., Schou, J., Hoeksema, J. T., et al. 2016, *SoPh*, **291**, 1887
Cranmer, S. R. 2009, *LRSP*, **6**, 3
Dowdy, J. F., Jr., Rabin, D., & Moore, R. L. 1986, *SoPh*, **105**, 35
Dunn, R. B., & Zirker, J. B. 1973, *SoPh*, **33**, 281
Efron, B. 1979, *AnStat*, **7**, 1
Efron, B., & Tibshirani, R. J. 1993, An Introduction to the Bootstrap (New York: Chapman and Hall)
Gabriel, A. H. 1976, *RSPTA*, **281**, 339
Gosling, J. T. 1996, *ARA&A*, **34**, 35
Gošić, M., Bellot Rubio, L. R., Orozco Suárez, D., Katsukawa, Y., & del Toro Iniesta, J. C. 2014, *ApJ*, **797**, 49
Hackenberg, P., Marsch, E., & Mann, G. 2000, *A&A*, **360**, 1139
Hassler, D. M., Dommisch, I. E., Lemaire, P., et al. 1999, *Sci*, **283**, 810
Heinemann, S. G., Temmer, M., Hofmeister, S. J., Veronig, A. M., & Vennerstrom, S. 2018, *ApJ*, **861**, 151
Hofmeister, S. J., Veronig, A., Reiss, M. A., et al. 2017, *ApJ*, **835**, 268
Iida, Y., Hagenaar, H. J., & Yokoyama, T. 2012, *ApJ*, **752**, 149
Kaiser, M. L., Kucera, T. A., Davila, J. M., et al. 2008, *SSRv*, **136**, 5
Krista, L. D., & Gallagher, P. T. 2009, *SoPh*, **256**, 87
Lemen, J. R., Title, A. M., Akin, D. J., et al. 2012, *SoPh*, **275**, 17
Levine, R. H. 1982, *SoPh*, **79**, 203
Pesnell, W. D., Thompson, B. J., & Chamberlin, P. C. 2012, *SoPh*, **275**, 3
Petrie, G. J. D., & Haislmaier, K. J. 2013, *ApJ*, **775**, 100
Petrovay, K., & Szakaly, G. 1993, *A&A*, **274**, 543
Pietarila Graham, J., Cameron, R., & Schüssler, M. 2010, *ApJ*, **714**, 1606
Pinto, R. F., Brun, A. S., & Rouillard, A. P. 2016, *A&A*, **592**, A65
Pinto, R. F., & Rouillard, A. P. 2017, *ApJ*, **838**, 89
Reiss, M., Temmer, M., Rotter, T., Hofmeister, S. J., & Veronig, A. M. 2014, *CEAB*, **38**, 95
Rotter, T., Veronig, A. M., Temmer, M., & Vršnak, B. 2012, *SoPh*, **281**, 793
Schou, J., Scherrer, P. H., Bush, R. I., et al. 2012, *SoPh*, **275**, 229
Schüssler, M. 2013, in Solar and Astrophysical Dynamos and Magnetic Activity (Cambridge: Cambridge Univ. Press), 95
Schüssler, M., & Vögler, A. 2008, *A&A*, **481**, L5
Schwenn, R. 2006, *SSRv*, **124**, 51
Solanki, S. K. 1993, *SSRv*, **63**, 1
Temmer, M., Hinterreiter, J., & Reiss, M. A. 2018, *JWSWC*, **8**, A18
Tu, C.-Y., Zhou, C., Marsch, E., et al. 2005, *Sci*, **308**, 519
Wang, Y.-M. 2009, *SSRv*, **144**, 383
Wang, Y.-M., Hawley, S. H., & Sheeley, N. R., Jr. 1996, *Sci*, **271**, 464
Wang, Y.-M., & Sheeley, N. R., Jr. 1990, *ApJ*, **355**, 726
Wiegelmann, T., & Solanki, S. K. 2004, *SoPh*, **225**, 227
Wiegelmann, T., Thalmann, J. K., & Solanki, S. K. 2014, *A&ARv*, **22**, 78
Wiegelmann, T., Xia, L. D., & Marsch, E. 2005, *A&A*, **432**, L1
Woolsey, L. N., & Cranmer, S. R. 2014, *ApJ*, **787**, 160